AIAA JOURNAL
Vol. 32, No. 7, July 1994

Computing Unsteady Shock Waves for Aeroacoustic Applications

Kristine R. Meadows*
NASA Langley Research Center, Hampton, Virginia 23681
David A. Caughey†
Cornell University, Ithaca, New York 14853
and
Jay Casper‡
ViGYAN, Inc., Hampton, Virginia 23666

The computation of unsteady shock waves, which contribute significantly to noise generation in supersonic jet flows, is investigated. The paper focuses on the difficulties of computing slowly moving shock waves. Numerical error is found to manifest itself principally as a spurious entropy wave. Calculations presented are performed using a third-order essentially nonoscillatory scheme. The effect of stencil biasing parameters and of two versions of numerical flux formulas on the magnitude of spurious entropy are investigated. The level of numerical error introduced in the calculation is quantified as a function of shock pressure ratio, shock speed, Courant number, and mesh density. The spurious entropy relative to the entropy jump across a static shock decreases with increasing shock strength and shock velocity relative to the grid, but is insensitive to Courant number. The structure of the spurious entropy wave is affected by the choice of flux formulas and algorithm biasing parameters. The effect of the spurious numerical waves on the calculation of sound amplification by a shock wave is investigated. For this class of problem, the acoustic pressure waves are relatively unaffected by the spurious numerical phenomena.

Introduction

THIS work is motivated by the knowledge that the presence of shocks in jet flows, on airfoils, and in supersonic combustion inlets significantly affects noise generation. Thus, the ability to accurately compute flows with moving shocks is necessary for direct simulation of sound generation in supersonic flows.

The numerical treatment of unsteady shocks for aeroacoustic applications is challenging. In addition to the usual numerical concerns of stability and accuracy, there are concerns of resolving disparate scales in the computation. First, there are disparities in amplitude. Large gradients exist at the shock, and because it is desirable to resolve the shock without Gibbs' oscillations, artificial dissipation is usually increased at the shock. However, small amplitude acoustic waves must also be resolved, and increasing artificial dissipation may overwhelm the acoustic perturbations. Second, there are disparate length scales which must be resolved for complete solution of the problem. The small shock excursion must be resolved for proper computation of the entropy, yet the acoustic and entropy waves have a much longer wavelength.

The Gibbs phenomenon produced by attempting to resolve a discontinuity on a finite mesh is well known, has been discussed widely in relation to steady shock calculations, and will not be addressed here. There is an additional oscillatory phenomenon which can manifest itself in the computation of slowly moving shocks. This additional oscillation resulting from the unsteady nature of slowly moving shocks has only recently been discussed in the literature,[1-3] and is investigated here to determine the nature of the spurious oscillations and the effect that these spurious numerical oscillations have on computing sound.

To simplify the analysis and better isolate difficulties in the numerical calculations, only one-dimensional and quasi-one-dimensional flows will be treated here. Thus, vorticity waves will not appear and emphasis will be on predicting the acoustic and entropy waves. Two model problems will be investigated: 1) a shock moving at a constant velocity in a one-dimensional flowfield, and 2) a shock wave disturbed by an upstream sound disturbance in a converging-diverging nozzle.

Spurious oscillations in unsteady computations of slowly moving shocks have been described by Woodward and Collela,[1] who observed the oscillations in computations of high-pressure ratio ($p_2/p_1 > 10^5$) shocks. These oscillations appear when the speed of the shock, relative to the mesh, is small compared to the maximum flow speed at the shock. Woodward and Collela suggested that additional numerical dissipation be added to the scheme at the shock, and explained that the reason for this spurious numerical behavior is that the shock transition layer alternates between being thick and thin as it passes through the mesh. Roberts[2] has noted that the oscillation phenomenon is not observed in discontinuous solutions of *scalar* equations. Roberts explains the oscillation in terms of the discrete shock structure and shows that among first-order flux-difference splitting schemes, Osher's approximate Riemann solver provides the smallest oscillations because the unsteady nature of the numerical shock structure in state space most closely approximates the true shock structure. Roberts observed spurious oscillation phenomenon in calculations for shock pressure ratios as low as 1.2 in calculations using first-order flux-difference splitting schemes. Lindquist and Giles[3] observed spurious oscillations in computations using a Jameson-style Runge-Kutta scheme with blended second- and fourth-difference artificial dissipation and also with a van Leer flux vector splitting algorithm for shock pressure

Received Sept. 28, 1993; revision received Feb. 22, 1994; accepted for publication Feb. 24, 1994. Copyright © 1994 by the American Institute of Aeronautics and Astronautics, Inc. No copyright is asserted in the United States under Title 17, U.S. Code. The U.S. Government has a royalty-free license to exercise all rights under the copyright claimed herein for Governmental purposes. All other rights are reserved by the copyright owner.

*Aerospace Engineer, Aeroacoustics Branch, Mail Stop 461. Member AIAA.

†Professor and Director, Sibley School of Mechanical and Aerospace Engineering. Associate Fellow AIAA.

‡Research Engineer, Advanced Technology Research Group, 30 Research Drive. Member AIAA.

ratios $1.5<p_2/p_1<2.1$. They described the oscillations in terms of the changing shock shape as the shock traverses the computational mesh, and found, as did Woodward and Collela, that the spurious oscillations could be reduced by smearing the shock over more computational cells.

The present authors have observed the spurious oscillations in computations using the classical MacCormack scheme, a recently developed high-order-accurate essentially nonoscillatory (ENO) scheme, and a recent implementation of Jameson's Runge-Kutta scheme which employs a symmetric total variation diminishing (TVD) matrix dissipation. Because the interest here is to compute sound generated by shocks and shock-fluid interactions, artificial dissipation is not explicitly increased over the solution domain because of the deleterious effect on the generation and propagation of sound in the solution. This has created some difficulties because the spurious oscillations are preserved in the high-order-accurate flow computations.

ENO schemes of the Godunov type rely on the solution of the Riemann problem for the calculation of numerical fluxes. The effect that two Riemann solvers have on the spurious oscillations will be described in the paper. In addition, because ENO schemes use an adaptive stencil to reduce spurious oscillations, modifications of this adaptive procedure will be examined. Finally, the effects of shock pressure ratio, Courant number, grid spacing, and shock speed on the amplitude and frequency of the spurious numerical oscillations will be described.

Algorithm: Essentially Nonoscillatory Scheme

During the course of this research, MacCormack, matrix dissipation TVD,[4,5] and ENO schemes were applied. However, in the interest of brevity, and because trends were similar for all of the algorithms considered, only the ENO results are presented in this paper.

The class of ENO schemes is relatively new[6] and is chosen because high-order accuracy is achieved in smooth portions of the flow, while spurious oscillations around flow discontinuities such as shocks are bounded. A brief discussion of the properties of ENO schemes is given hereafter, but interested readers are referred to Refs. 6 and 7 for details.

An ENO solution operator E_h is rth-order accurate in the sense of local truncation error

$$E_h u^n = u^{n+1} + \mathcal{O}(h^{r+1})$$

where $u(x)$ is the sufficiently smooth exact solution, and h is the cell spacing. The distinguishing property of ENO schemes is that spurious oscillations near discontinuities in u are bounded. For the one-dimensional scalar case, this can be written:

$$TV(E_h u) = TV(u) + \mathcal{O}(h^{1+q})$$

for some $q>0$, where $TV(u)$ is the total variation of u as a function of x.

Bounding oscillations near discontinuities is accomplished in ENO schemes through the use of an adaptive stencil. Because the stencil used for discretizing the differential equations adapts to the solution, schemes based on the ENO property may be thought of as adaptive filters or nonlinear algorithms.

ENO schemes minimize numerical oscillations around discontinuities by using data from the smoothest part of the flow. At each cell, a searching algorithm determines which portion of the surrounding flow is smoothest. The stencil spanning this portion of the flow is then used to construct a higher order accurate, conservative interpolation to determine the variables at the cell interfaces.

In this particular finite volume implementation, the interpolation operator is applied to the cell averaged characteristic variables, and the accuracy in space and in time is third order. Time integration is accomplished by the use of a third-order, three-stage Runga-Kutta scheme discussed by Shu and Osher.[7] The algorithm is applied to the conservation law form of the equations so that shocks are captured in the computations and no shock fitting is required to enforce the Rankine-Hugoniot jump relations across shocks which appear in the solution.

Stencil Biasing Parameters

ENO schemes can achieve high-order accuracy in smooth regions and capture shocks without oscillations by the use of adaptive stenciling. As the ENO schemes were originally presented in Ref. 6, the stencil shifts freely due to any detection of a numerical gradient. The direction of the stencil shift is determined by the magnitudes of the neighboring divided differences. The stencil shifts away from the larger differences. However, a loss of accuracy can occur when this freely adaptive algorithm is used.[8,9] Shu[10] has suggested that the stencil be biased toward a preferred stencil, the one that makes the scheme stable in the sense of linear stability analysis. The stencil is allowed to shift only when one neighboring difference is larger than the other by some factor. This factor will be referred to as the bias parameter.

Even when a bias parameter is used, there may be a loss of accuracy when all of the numerical gradients in a region are small, but some are orders of magnitude larger than others. Atkins[11] has suggested the use of another parameter, which serves as a threshold, to force the shift to the preferred stencil whenever neighboring differences are small, regardless of their relative magnitudes. This parameter will be referred to as the threshold parameter.

Essentially Nonoscillatory Flux Computation

ENO schemes of the Godonov type rely on the solution of the Riemann problem to calculate numerical fluxes. Two methods of computing the fluxes across the cell interfaces are evaluated in this paper. The first is due to Roe,[12] and the second is due to Osher and Solomon.[13]

Consider a system of hyperbolic equations,

$$\frac{\partial U}{\partial t} + \frac{\partial F}{\partial x} = 0$$

where U is a vector of J components, and F is a J component differentiable function of U.

Roe's approximate Riemann solver determines the change in flux by finding a mean Jacobian matrix $\tilde{A}$ which satisfies:

$$\Delta F = \tilde{A}\,\Delta U$$

where Δ represents the difference between any two states in solution space. The matrix $\tilde{A}$ is required to have a complete set of right eigenvectors and to reduce to the exact Jacobian when the states to the left and the right are equal: $\tilde{A}(U, U) = (\partial F/\partial U)(U)$. If $\tilde{\lambda}_{(j)}$, $\tilde{r}^{(j)}$, and δw_j are the jth eigenvalue, right eigenvector, and inner product of the jth left eigenvector with ΔU, respectively, the preceding equation can be written:

$$\Delta F = \sum_{j=1}^{J} \tilde{r}^{(j)} \tilde{\lambda}_{(j)} \delta w_j$$

The flux at the cell interface is written:

$$f = \frac{1}{2}(F_L + F_R) - \frac{1}{2}\sum_j |\tilde{\lambda}_{(j)}| \delta w_j \tilde{r}^{(j)}$$

where F_L and F_R are the values of the fluxes to the left and right of the interface, respectively. Roe gives the expressions for $\tilde{\lambda}$, $\tilde{r}$ and δw_j for the Euler equations in Ref. 12.

Osher's approximate Riemann solver computes fluxes in state space rather than physical space. The flux difference between the left and right states is written:

$$\Delta F = \int_{U_L}^{U_R} \frac{\partial F}{\partial U}\, dU$$

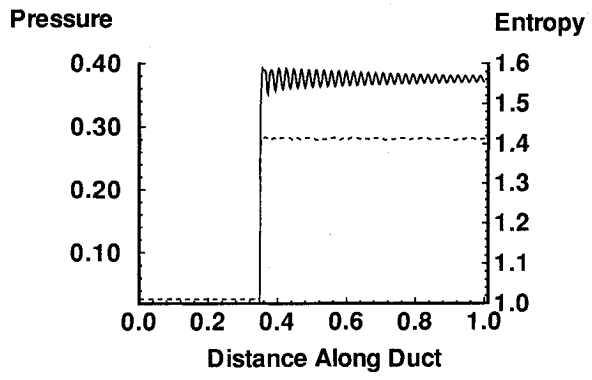

Fig. 1 Pressure and entropy as functions of distance along duct: shock speed = 0.05, shock pressure ratio = 10.33; dashed line represents pressure, solid line represents entropy.

where the integral is evaluated along an arbitrary path Γ in state space.

The flux at the cell interface is given by:

$$f = \frac{1}{2}(F_L + F_R) - \frac{1}{2}\sum_j \int_{\Gamma(j)} |\lambda_{(j)}| r^{(j)} \lambda \, dU$$

The evaluation of the preceding integral requires knowledge of the states along each subpath $\Gamma(j)$ and any sonic states that occur. Osher and Solomon[13] solve for these states explicitly for the Euler equations.

Model Problem: Slowly Moving Shock in a Duct

Analysis: Exact Solution

The governing equations for the inviscid, compressible flow in a duct are the one-dimensional Euler equations,

$$\frac{\partial U}{\partial t} + \frac{\partial F}{\partial x} = 0 \tag{1}$$

where U is the vector of conserved variables $[\rho, \rho u, \rho e]^T$, and F is the flux vector $[\rho u, \rho u^2 + p, (\rho e + p)u]^T$. Standard notation is used; ρ is density, u is velocity, e is total energy per unit mass, and p is pressure.

Consider these equations along the duct length $0 \le x \le L$, for $t > 0$, with the initial condition:

$$U(x, 0) = \begin{cases} U_1 & x < x_s \\ U_2 & x > x_s \end{cases} \tag{2}$$

where the constant states 1 and 2 respresent the flow upstream and downstream of a shock, respectively, and x_s is the shock position.

The nontrivial solution to this equation with the intial condition (2) is a flowfield with a shock moving at constant velocity u_s, which satisfies

$$F(U_2) - F(U_1) = u_s(U_2 - U_1)$$

Results

The unsteady, compressible, inviscid flow in the duct is solved by numerical integration of the one-dimensional Euler equations. The entire supersonic flowfield at the inflow boundary is prescribed. The static pressure at the downstream boundary is prescribed. Variables are normalized by the duct length, stagnation pressure, and stagnation sound speed.

Computations have been performed over a range of shock pressure ratios and shock speeds, but in the interest of brevity, only one typical calculation is shown here. The calculations were performed on a 512-cell grid at a Courant number of 1. Unless noted otherwise, calculations are performed using Roe's flux solver and both the bias parameter and threshold parameter are on, meaning that the stencil is biased toward the preferred one, and a threshold limit is set. Figure 1 illustrates the spurious oscillations observed with the third-order ENO scheme for a case in which the pressure ratio across the shock is 10.333 and the shock is moving to the left at a speed of 0.05. Figure 1 shows the pressure and entropy distributions in the duct after the shock has moved 15% of the duct length. Entropy is measured by the quantity $s = p/\rho^\gamma$. Although there were no oscillations at the shock in the initial shock position, once the shock begins to move, spurious waves develop in the flow solution. The oscillation is seen primarily in the entropy wave; the pressure wave is relatively unaffected.

The spurious error is due to the discrete motion of the shock moving through the mesh. When the shock is located at a cell interface, it is extremely thin. As it moves through the cell interior, it smears out, weakens in strength, and entropy and pressure waves convect downstream. If the shock passing frequency is defined as the frequency associated with the shock passing through a cell, $f_{\text{shock}} = u_s/\Delta x$ where Δx is the grid spacing, and u_s is the shock speed relative to the grid, the wavelengths associated with the pressure and entropy waves, λ_p and λ_s, are determined by

$$\lambda_p = \frac{(u_2 + a_2)}{f_{\text{shock}}} = \frac{(u_2 + a_2)\Delta x}{u_s} \tag{3}$$

$$\lambda_s = \frac{u_2}{f_{\text{shock}}} = \frac{u_2 \Delta x}{u_s} \tag{4}$$

where u_2 and a_2 are the downstream velocity, relative to the shock, and sound speed, respectively. When adequately resolved on the mesh, the spurious pressure and entropy waves measured in the numerical computations compare well with the wavelengths λ_p and λ_s described by the preceding equations. For example, the wavelength λ_s of the entropy wave in Fig. 1 is computed $\lambda_s \approx 0.550 * 0.00195/0.05 \approx 0.021$. Inspection of the figure verifies this result. Because the error introduced by the slow shock motion is manifest primarily in the entropy, further discussion will focus on this flow variable.

A series of calculations, for the same $p_2/p_1 = 10.333$ shock strength, illustrates the effect of shock speed on the behavior of the spurious oscillations. These calculations were performed on a 512-cell grid at a Courant number of 1.0. Figure 2 shows the entropy distributions in the tube after the shock has moved to the left for a normalized time of 3.0 for shock speeds of 0.02, 0.05, and 0.15. For clarity, the entropy distributions are offset by a constant value of 0.1. The entropy upstream of the shock is 1.0. The perturbations are again visible in the entropy distribution, and the wavelengths of these perturbations are consistent with Eq. (4). The long wavelength disturbances at the lowest shock speeds are only slightly damped downstream of the shock, whereas the short wavelength disturbances at high shock speeds are damped very quickly by the dissipation in the scheme. This, of course, explains why these disturbances are not seen when the shock speed through the mesh is comparable to the flow speed.

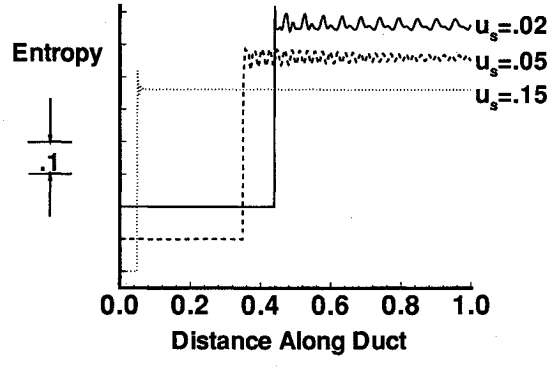

Fig. 2 Entropy as a function of distance along duct and shock speed: shock speeds = 0.02, 0.05, 0.15, shock pressure ratio = 10.33.

Effect of Shock Speed

Figure 3 summarizes the effect of the shock velocity relative to the grid on the maximum amplitude of the spurious entropy. The ratio of the magnitude of the maximum zero-to-peak entropy error amplitude to the jump in entropy across the shock is plotted as a function of the ratio of the shock velocity (normalized by upstream stagnation sound speed) to the upstream Mach number. These calculations were performed for a shock moving to the right at shock speeds from 0 to 5.0 on a 256-cell mesh. The spurious entropy amplitude is machine zero when the shock is stationary relative to the grid, increases to a maximum when $0.005 < u_s/M < 0.1$, and decreases as the ratio of u_s/M increases further.

Effect of Shock Strength

Figure 3 also illustrates that the magnitude of the maximum spurious entropy amplitude is a function of shock pressure ratio. As the shock strength increases, the magnitude of entropy error, relative to the static entropy jump, decreases. In the weak shock case, $M = 1.1$, the spurious oscillations are close to 100% of the static jump in entropy over a range of shock speeds.

Effect of Courant Number

A sequence of calculations were performed with Courant numbers between 0.1 and 1.0 (the stability limit[7]) to determine the effect of Courant number on the spurious entropy. Neither the amplitude nor the wavelength of the spurious oscillations is found to be sensitive to the Courant number. This is consistent with the results reported by Roberts for flux-difference splitting schemes.[2]

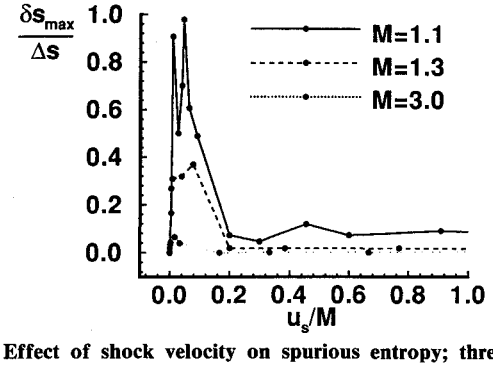

Fig. 3 Effect of shock velocity on spurious entropy; three shock strengths are shown.

Effect of Stencil Biasing Parameters

In this section the effects of the stencil biasing parameters on the spurious entropy are investigated. To illustrate the effects of these parameters on the algorithm, Fig. 4 shows a space-time diagram of the stencil used in the ENO algorithm for four combinations of stencil biasing parameters: case (a) threshold on, bias on; case (b) threshold off, bias on; case (c) threshold off, bias off; and case (d) threshold on, bias off. For clarity, the space-time diagrams are limited to the region near the shock, and the total number of cells in the computations was reduced to 256. The shock is initially located at $x = 0.5$ and moves with a velocity of 0.01 to the left. The upstream Mach number is 1.3. For cases (a) and (d), the threshold is on, and a centered stencil is used for the majority of the computational space. The centered stencil is the linearly stable stencil in this case. Cells on either side of the shock use downwind or upwind stencils as appropriate. For cases (b) and (c), the threshold parameter is off, and there is a great deal more stencil shifting in the smooth regions of the flow. It is interesting to note that the stencils in these two figures follow entropy and acoustic wave paths downstream of the shock. The stencil traces for these wave paths have slopes corresponding to acoustic and convecting wave speeds.

Plots of the entropy corresponding to the cases (a–d) are shown in Fig. 5. The entropy distributions are offset by a constant value of 0.0075 and the numerical values of entropy are removed from the vertical axis for clarity. The entropy value upstream of the shock is 1.0, and the space between tick marks on the vertical axis corresponds to an entropy difference of 0.005. The entropy fluctuations are smallest for case b. The biasing parameters affect the structure of the entropy wave, although the wavelength is the same for all cases.

Effect of Mesh Spacing

The effect of the mesh spacing is illustrated by comparing Figs. 5 and 6. The results presented in Fig. 6 are for the same physical problem as that in Fig. 5, but the mesh is highly refined (1024 cells). As in Fig. 5, the entropy distributions in Fig. 6 are offset by a constant of 0.0075 and the numerical values of entropy are removed from the vertical axis for clar-

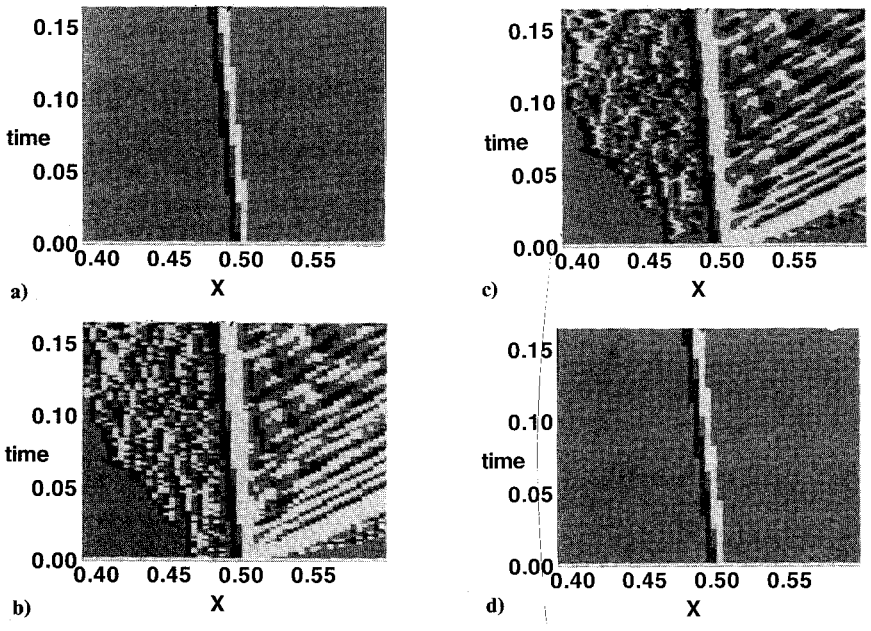

Fig. 4 Effect of stencil biasing parameter and threshold parameter on stencil; white represents a downwind stencil, black represents an upwind stencil, gray represents a centered stencil: case a) biasing on, threshold on; case b) biasing on, threshold off; case c) biasing off, threshold off; case d) biasing off, threshold on. 256 cells.

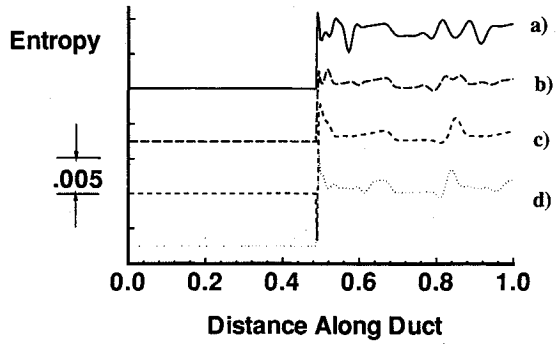

Fig. 5 Entropy as a function of duct distance for various combinations of biasing and threshold parameters: case a) biasing on, threshold on; case b) biasing on, threshold off; case c) biasing off, threshold off; case d) biasing off, threshold on. 256 cells.

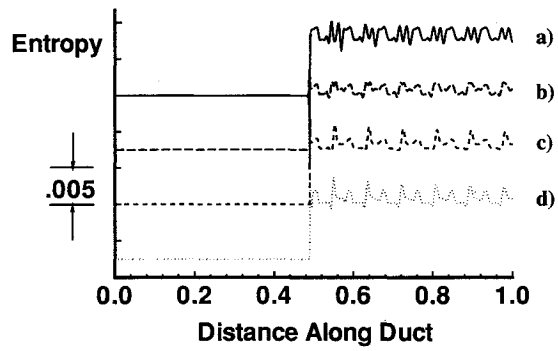

Fig. 6 Entropy as a function of duct distance for various combinations of biasing and threshold parameters: case a) biasing on, threshold on; case b) biasing on, threshold off; case c) biasing off, threshold off; case d) biasing off, threshold on. 1024 cells.

ity. The difference between tick marks is 0.005. Refining the mesh reduces the magnitude of entropy oscillation and shows the effect of the biasing parameters more distinctly. Each combination of biasing parameters has a unique spurious entropy pattern. Case (a) is highly oscillatory, with multiple frequencies per wavelength of the oscillation. Case (b) has the smallest amplitude of entropy peaks. Case (c) has the fewest peaks per period of spurious oscillation, but the amplitude of the largest peak is high. Case (d) has large entropy peaks as well as multiple frequencies per oscillation. Although all of the results show significant entropy error, the results obtained by biasing the stencil and turning the threshold off [case (b)] provide the lowest amplitude of entropy error.

Another effect of the mesh spacing is the reduction in the wavelength of the spurious entropy. In Fig. 5, the wavelength of spurious entropy computed by Eq. (4) is $\lambda_s \approx 0.34$. Refining the mesh in Fig. 6 reduces this wavelength to $\lambda_s \approx 0.086$. The number of points per wavelength of the spurious entropy wave is the same for both computations, because u_2/u_s is constant.

Figure 7 is included to show the effect of the Osher flux solver on the spurious entropy. The result is shown only for case b because other cases provided similar results. The effect of the Osher solver on the spurious entropy is to remove one of the peaks in the entropy wave each oscillation wavelength.

Summary: Slowly Moving Shock in a Duct

This section has illustrated numerical difficulties in computing slowly moving shocks. Although changes in flux computation, algorithmic parameters, and Courant number were made in an effort to remove these spurious entropy waves, they persisted.

Calculations of supersonic jet noise will often have shocks moving slowly relative to the grid. Although the results presented thus far have shown that spurious entropy exists in calculations with slowly moving shocks, it has also been noted that spurious pressure waves are very small in amplitude. Thus, the next section will focus on calculating sound wave amplification through shocks.

Model Problem: Interaction of Sound Wave and Shock

Analysis

Consider now the second model problem of the interaction of a sound wave with a shock in a quasi-one-dimensional nozzle. A pressure perturbation $\delta p_1 = \epsilon p_i$, where p_i is the inlet static pressure, is introduced upstream of the shock. The pressure perturbation propagates through the shock, causing the shock to move. The sound wave is transmitted through the shock, and its amplitude is changed to δp_2. The motion of the shock creates an entropy disturbance δs_2 which convects downstream.

Within the context of linear theory, only entropy and acoustic waves exist in one- or quasi-one-dimensional flow. Linear analyses of the interaction of small disturbances have been made independently by Blokhintsev[14] and others.[15-17] For an acoustic disturbance incident on the supersonic side of the shock, Landau and Lifschitz[18] report that the ratio of transmitted to incident sound waves may be closely approximated by:

$$\frac{\delta p_2}{\delta p_1} = \frac{(M_1+1)}{(M_2+1)} * \frac{2(\gamma-1)M_1M_2^2(M_1^2-1)-(M_1+1)[(\gamma-1)_1^2+2]}{2(\gamma-1)M_2^2(M_1^2-1)-(M_2+1)[(\gamma-1)M_1^2+2]}$$

where M_1 is the Mach number upstream of the shock, M_2 is the Mach number downstream of the shock, and γ is the ratio of specific heats of the fluid.

This result is based on linear theory in which disturbance amplitudes are assumed to be small. To determine the range for which the linear result is valid, one may compute the ratio of disturbance pressures across the shock by considering the iterative solution to the Riemann problem. The Riemann anal-

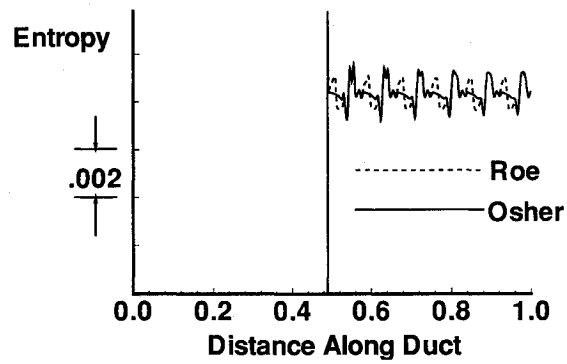

Fig. 7 Entropy as a function of distance along duct length for Roe and Osher flux solvers; biasing on, threshold off.

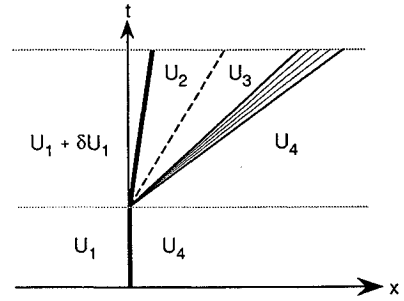

Fig. 8 Diagram of the quasisteady Riemann problem analysis for sound-shock interaction: bold line represents shock, dashed line represents entropy wave, and lines between states 3 and 4 represent acoustic wave.

ysis is performed by considering the space-time diagram illustrated in Fig. 8. Initially a steady shock wave separates states 1 and 4. At some time Δt, a disturbance is introduced upstream of the shock which moves the shock and produces acoustic and entropy waves downstream. Knowing the initial states 1 and 4, and the incident perturbation amplitude, and utilizing the facts that acoustic waves are isentropic and entropy waves introduce no pressure perturbation, the ratio of the perturbed states 2 and 1 may be found by numerical iteration. For an incident sound wave, the ratio $\delta p_2/\delta p_1$ is of interest and is compared with the linear theory result in Fig. 9 for several perturbation amplitudes and shows excellent agreement for perturbation amplitudes less than $\epsilon = 10^{-1}$. (Results for $\epsilon \leq 10^{-2}$ are visually indistinguishable from the Blokhintsev line.) Even for perturbation amplitudes on the order of $\epsilon = 1.0$, there is only a 10% difference between the solutions at $M = 3$.

Combining the expression for $\delta p_2/\delta p_1$ with the Rankine-Hugoniot shock jump relations, one may calculate similar expressions for the fluctuations in density and entropy downstream. These relations are plotted in Fig. 10. The ratios presented in Fig. 10 were computed using a perturbation amplitude of $\epsilon = 10^{-3}$. This figure shows that the pressure fluctuation is most significant over a wide range of Mach numbers. The entropy fluctuations downstream of the shock are very small; the quantity $\delta s/\Delta s$ is on the order of ϵ, except near $M = 1$ where $\Delta s \to 0$.

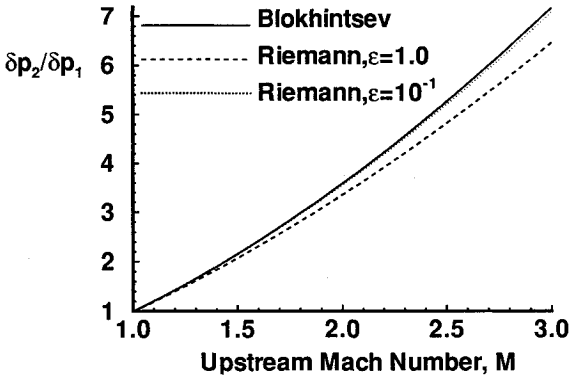

Fig. 9 Pressure perturbation as function of upstream Mach number.

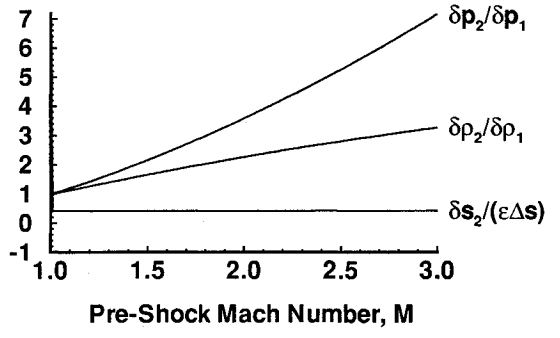

Fig. 10 Perturbation ratios as a function of upstream Mach number.

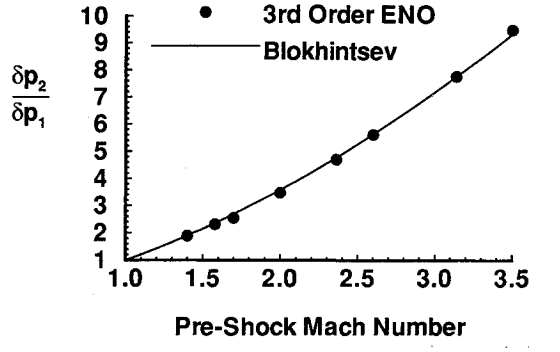

Fig. 11 Pressure perturbation ratio as a function of upstream Mach number.

Numerical Issues

The equations governing the interaction of a sound disturbance and a shock wave in a nozzle are:

$$\frac{\partial U}{\partial t} + \frac{\partial F}{\partial x} = Q$$

where U is the vector of conserved variables $[\rho A \ \rho u A \ \rho e A]^T$, F is the flux vector, $[\rho u A \ (\rho u^2 + p)A \ (\rho e + p)uA]^T$, A is the area of the nozzle, and Q is a source vector due to the area variation $[0, p\,(dA/dx), 0]^T$.

These equations are solved with the third-order-accurate ENO scheme. Finite wave conditions[19] are employed at the boundaries so that a steady shock is established in the nozzle. Variables are normalized by upstream stagnation pressure and sound speed, and by the nozzle length. To induce unsteady flow through the nozzle, the inflow boundary condition is perturbed sinusoidally and isentropically. The pressure perturbation at the inlet is prescribed as

$$\delta p(t) = \epsilon p \sin \omega t, \qquad t > 0$$

where ϵ and ω are the normalized amplitude and frequency of the perturbation. The pressure perturbation introduces an acoustic wave at the inlet which propagates at a velocity equivalent to the local velocity plus the local speed of sound.

Computation of Sound Amplification in Quasi-One-Dimensional Flows

Consider now the computation of shock motions in ducts of varying cross-sectional area. A steady, shocked flow is first established in a quasi-one-dimensional nozzle, designed to produce a linear Mach number distribution when the flow is isentropic and fully expanded. A perturbation is introduced at the nozzle inlet, propagates downstream, and passes through the shock. Thus, for this time-dependent problem, an acoustic wave exists upstream of the shock, and both acoustic and entropy waves exist downstream. However, the results in this section will focus only on the acoustic waves, because the spurious numerical entropy waves are of larger amplitude than the physical entropy waves.

To quantify the effect of Mach number on the perturbation amplification and validate the computations, the numerically determined pressure perturbation amplitude ratio is compared in Fig. 11 with the results of linear theory over a range of Mach numbers for a perturbation with $\epsilon = 10^{-5}$. This perturbation amplitude is selected because it is well within the linear regime. The normalized acoustic perturbation wave number at the inflow boundary is set to 4. Numerical results for Mach numbers between 1.4 and 3.5 are presented here. In these computations, the acoustics perturbations are resolved with 22–27 cells per wavelength, depending on the particular case being calculated. The results from the third-order ENO scheme and linear theory compare well.

Conclusions

The computation of slowly moving shock waves produces spurious, numerical entropy. The spurious entropy is a function of the algorithm used in the calculation, and, as seen by the modifications made to the ENO scheme, even slight changes in a basic algorithm can produce marked changes in the structure of the spurious entropy. It is interesting to note that this phenomenon has been observed by the authors in implementing the MacCormack scheme, ENO schemes, and a

matrix dissipation Runge-Kutta scheme, and by others using flux vector splitting schemes,[3] flux-difference splitting schemes with Gudonov, Roe, and Osher flux solvers,[2] and piecewise-parabolic methods.[1] Spurious entropy normalized by the entropy jump across the shock decreases with increasing shock strength and increasing shock velocity, but is insensitive to Courant number. The amplitude of spurious entropy perturbations is relatively unaffected by the type of flux solver used, but the Osher solver reduces the number of peaks in the spurious entropy wave form.

Because the amplitude of the spurious entropy wave is a function of the shock speed relative to the grid, the obvious method of eliminating the spurious wave is to move the computational grid with the shock during the calculation. Although this shock tracking is not difficult in one-dimensional problems, it is considered unreasonable for the multidimensional problems of practical interest, and was not implemented during the course of this research. Another approach to reducing the spurious entropy is to increase the dissipation of the algorithm, as suggested by Woodward and Collela. This was not implemented, because the added dissipation would affect the acoustic waves as well as the entropy.

Fortunately, acoustic pressure waves for this class of problems seem unaffected by the spurious entropy. Calculations to determine the perturbation pressure ratio across unsteady shocks have been performed for flows in quasi-one-dimensional nozzles, and these results are validated by linear theory over a range of upstream Mach numbers of practical interest for supersonic jets.

References

[1]Woodward, P., and Collela, P., "The Numerical Simulation of Two-Dimensional Fluid Flow Through Shocks," *Journal of Computational Physics,* Vol. 54, No. 1, 1984, pp. 115–173.

[2]Roberts, T. W., "The Behavior of Flux Difference Splitting Schemes Near Slowly Moving Shock Waves," *Journal of Computational Physics,* Vol. 90, No. 1, 1990, pp. 141–160.

[3]Lindquist, D. R., and Giles, M. B., "On the Validity of Linearized Unsteady Euler Equations with Shock Capturing," AIAA Paper 91-1598, June 1991.

[4]Jorgenson, P., and Turkel, E., "Central Difference TVD and TVB Schemes for Time Dependent and Steady State Problems," AIAA Paper 92-0053, Jan. 1992.

[5]Caughey, D. A., "Implicit Multigrid Euler Solutions with Symmetric Total-Variation-Diminishing Dissipation," *Proceedings of the AIAA 11th Computational Fluid Dynamics Conference* (Orlando, FL), AIAA, Washington, DC, 1993, pp. 676–684.

[6]Harten, A., Enquist, B., Osher, S., and Chakravarthy, S. R., "Uniformly High Order Accurate Essentially Non-oscillatory Schemes, III," *Journal of Computational Physics,* Vol. 71, No. 2, 1987, pp. 231–303.

[7]Shu, C.-W., and Osher, S., "Efficient Implementation of Essentially Non-Oscillatory Shock-Capturing Schemes," *Journal of Computational Physics,* Vol. 77, No. 2, 1988, pp. 439–471.

[8]Rogerson, A. M., and Meiberg, E., "A Numerical Study of the Convergence Properties of ENO Schemes," *Journal of Scientific Computing,* Vol. 5, No. 2, 1990, pp. 151–167.

[9]Casper, J., Shu, C.-W., and Atkins, H. L., "A Comparison of Two Formulations for High-Order Accurate Essentially Non-Oscillatory Schemes," AIAA Paper 93-3338, July 1993.

[10]Shu, C., "Numerical Experiments on the Accuracy of ENO and Modified ENO Schemes," *Journal of Scientific Computing,* Vol. 5, No. 2, 1990, pp. 127–150.

[11]Atkins, H. L., "High-Order ENO Methods for the Unsteady Compressible Navier-Stokes Equations," AIAA Paper 91-1557, June 1991.

[12]Roe, P. L., "Approximate Riemann Solvers, Parameter Vectors, and Difference Schemes," *Journal of Computational Physics,* Vol. 43, No. 2, 1981, pp. 357–372.

[13]Osher, S., and Solomon, F., "Upwind Difference Schemes for Hyperbolic Systems of Conservation Laws," *Mathematics of Computation,* Vol. 38, No. 158, April 1982, pp. 339–374.

[14]Blokhintsev, D., "Sound Receiver in Motion," *Comptes Rendus (Doklady) De L'Academe Des Sciences De L'URSS,* Vol. XLVII, No. 1, 1945, pp. 95–102.

[15]Burgers, J. M., "On the Transmission of Sound Waves Through a Shock Wave," *Koninklijke Nederlandische Akademie van Wetenschappen,* Vol. XLIX, No. 3, 1946, pp. 273–281.

[16]Moore, F. K., "Passage of Flow Disturbances Through a Duct Containing Screens, Shocks, or Contractions," *Proceedings of the 3rd Midwestern Conference on Fluid Mechanics,* Univ. of Minnesota, Minneapolis, MN, 1953, pp. 193–217.

[17]Powell, A., "One-dimensional Treatment of Weak Disturbances of a Shockwave," *Aeronautical Research Council Current Papers,* CP No. 441, 1959.

[18]Landau, L. D., and Lifschitz, E. M., *Fluid Mechanics,* Pergamon, New York, 1959.

[19]Atkins, H. L., and Casper, J., "Non-Reflective Boundary Conditions for High Order Methods," AIAA Paper 93-0152, Jan. 1993.